


Cite this: *RSC Adv.*, 2021, 11, 21057

Metal oxide/CeO₂ nanocomposites derived from Ce-benzene tricarboxylate (Ce-BTC) adsorbing with metal acetylacetonate complexes for catalytic oxidation of carbon monoxide†

Dongren Cai, * Bin Chen, Zhongliang Huang, Xiaoli Zeng, Jingran Xiao, Shu-Feng Zhou and Guowu Zhan *

Herein, a series of metal oxide/CeO₂ (M/CeO₂) nanocomposites derived from Ce-benzene tricarboxylate (Ce-BTC) adsorbing with different metal acetylacetonate complexes were prepared for CO oxidation under four different CO gas atmospheres. It was demonstrated that Cu/CeO₂ exhibited the highest catalytic activity and stability in CO oxidation. Remarkably, both O₂ selectivity and CO selectivity to CO₂ are 100% in most of the investigated conditions. Several analytical tools such as N₂ adsorption–desorption and powder X-ray diffraction, were employed to characterize the prepared catalysts. In addition, the excellent catalytic performance of Cu/CeO₂ in CO oxidation was revealed by H₂ temperature-program reduction experiment, X-ray photoelectron spectroscopy, and *in situ* diffuse reflectance infrared Fourier transform spectroscopy. The result showed that high oxygen vacancy and high CO adsorption capacity (Cu⁺–CO) caused by the electron exchanges of Cu²⁺/Cu⁺ and Ce³⁺/Ce⁴⁺ pairs (Ce⁴⁺ + Cu⁺ ⇌ Ce³⁺ + Cu²⁺) are two key factors contributing to the high oxidation performance of Cu/CeO₂ catalyst.

Received 28th April 2021
Accepted 5th June 2021

DOI: 10.1039/d1ra03319k

rsc.li/rsc-advances

1. Introduction

The removal of trace carbon monoxide (CO) from the bulk gas has become the key step for the development of clean energy (like fuel cells that utilize reformat gas as the fuel), and environmental protection (like treatment of automobile exhaust gas) in recent years.^{1–3} One of the most effective methods to remove CO from the bulk gas is the catalytic oxidation of CO, which converts CO to carbon dioxide (CO₂) directly.^{1,4,5} Compared to other methods (like water–gas shift reaction), this technique offers various benefits of low cost, ease of implementation, and thorough removal of CO.⁶ To complete the process of CO oxidation, preparing a highly active and stable catalyst is of vital importance.^{7,8}

Up to now, the potential catalysts for CO oxidation have been mainly concentrated on the noble metal (Ag, Au, Pt, *etc.*)/metal oxide (support) and metal oxide (active component)/metal oxide (support) (Co₃O₄/Al₂O₃, CuO/CeO₂, *etc.*).^{9–12} The noble metal always has an excellent performance in CO oxidation, but the high cost and low availability hinder the wide applications. Therefore, more attention has shifted to the metal oxide (active component)/metal oxide (support). The metal oxide (active component)/metal oxide (support)

are usually synthesized by impregnation, co-precipitation, deposition, sol–gel, *etc.* Although the catalyst forming can be effectively controlled, the dispersion of metal sites in the whole catalyst is poor, resulting in the sintering and deactivation easily during the reaction.^{13,14} As a result, the uniform dispersion of metal sites is essential to catalyst design for CO oxidation.

Metal–organic frameworks (MOFs) are organic–inorganic hybrid materials formed by self-assembly of metal ions (or clusters) and organic ligands through coordination bonds, which have been applied in gas separation, gas storage, drug delivery, and even catalysis in recent years.^{15–17} What more noteworthy is that MOFs can be used as a sacrificial template or precursor for the preparation of other porous materials (metal oxide, metal oxide/metal oxide, and so forth) *via* thermal decomposition because of their unique structure and textural property.^{18,19} In general, the derived metal oxides maintain the original morphology of MOFs, and own a large specific surface area and pore volume. Furthermore, the uncoordinated organic sites (like carboxyl, –COOH) on MOFs have strong adsorption capacity for transition metal ions, which can make the transition metal (M) uniformly enrich in MOFs, forming precursor M/MOFs. The direct calcination of M/MOFs would lead to the formation of the multicomponent metal oxides, which can be used as an excellent catalyst for CO oxidation.

Interestingly, the transition metal acetylacetonates (M(acac)_x) have been proved to be a good precursor for element doping.^{20–22} For example, based on the hydrogen bonding

College of Chemical Engineering, Huaqiao University, 668 Jimei Blvd, Xiamen, Fujian, 361021, P. R. China. E-mail: 15506@hqu.edu.cn; gwzhan@hqu.edu.cn

† Electronic supplementary information (ESI) available: Reactor image, pore size distribution, FT-IR, SEM images and TEM images. See DOI: 10.1039/d1ra03319k



interaction and ligand exchange mechanism, Kuśtrowski *et al.* successfully loaded $\text{Cu}(\text{acac})_2$, $\text{Fe}(\text{acac})_3$, and $\text{Cr}(\text{acac})_3$ on siliceous support.²¹ The research conducted by Vital *et al.* also revealed that $\text{M}(\text{acac})_x$ can be immobilized on amino-functionalized active carbon support.²² In view of this situation, the $\text{M}(\text{acac})_x$ can be used as the precursor of the active component to be doped into MOFs for improving the dispersion. Not only the active component but also the support plays an important part in determining the catalytic activity due to the effects of surface area, active component dispersion, and interactions with active component.¹ Cerium dioxide (CeO_2) is considered as excellent support for CO oxidation due to the huge oxygen storage and good redox ability. Besides, CeO_2 can improve the dispersion of the active metal components *via* the metal-support interface, which also enhances the anti-sintering ability of the metals.^{23–25} Therefore, CeO_2 derived from Ce-MOF (like Ce-BTC) would be highly desirable support material for CO oxidation.

Based on the above statements, herein, we prepared a variety of M/CeO_2 (multicomponent metal oxides) by using Ce-BTC adsorbing with metal acetylacetonate complexes as precursors. The catalytic performances of prepared M/CeO_2 were evaluated in CO oxidation under four different gas atmospheres (*e.g.*, dry, wet, H_2 -rich, and wet + H_2 -rich conditions). The prepared M/CeO_2 were characterized by N_2 adsorption-desorption, powder X-ray diffraction (XRD), inductively couple plasma-optical emission spectrometry (ICP-OES), thermogravimetric analysis (TGA), scanning electron microscopy (SEM), transmission electron microscopy (TEM), high-resolution transmission electron microscopy (HRTEM), and X-ray photoelectron spectroscopy (XPS). The interactions of active components and support were revealed by H_2 temperature-program reduction experiments (H_2 -TPR). Besides, *in situ* diffuse reflectance infrared Fourier transform spectroscopy (DRIFTS) was used to reveal the reaction process of CO oxidation over M/CeO_2 catalysts.

2. Experimental section

2.1 Chemicals

The chemicals used in this study were as follows: cerium nitrate hexahydrate ($\text{Ce}(\text{NO}_3)_3 \cdot 6\text{H}_2\text{O}$, 99.99%, Admas), trimesic acid ($\text{H}_3\text{-BTC}$, $\text{C}_6\text{H}_6\text{O}_6$, 99%, Admas), polyvinylpyrrolidone (PVP, MW: 50 000–60 000, Admas), ethanol ($\text{CH}_3\text{CH}_2\text{OH}$, 99.5%, Guoyao), *N,N*-dimethylformamide (DMF, $\text{HCON}(\text{CH}_3)_2$, 99.5%, Aladdin), cupric(II) acetylacetonate ($\text{Cu}(\text{acac})_2$, $\text{C}_{10}\text{H}_{14}\text{O}_4\text{Cu}$, 98%, Admas), nickel(II) acetylacetonate ($\text{Ni}(\text{acac})_2$, $\text{C}_{10}\text{H}_{14}\text{O}_4\text{Ni}$, 98%, Admas), cobalt(II) acetylacetonate ($\text{Co}(\text{acac})_2$, $\text{C}_{10}\text{H}_{14}\text{O}_4\text{Co}$, 99%, Admas), iron(III) acetylacetonate ($\text{Fe}(\text{acac})_3$, $\text{C}_{15}\text{H}_{21}\text{O}_6\text{Fe}$, 98%, Admas), copper nitrate trihydrate ($\text{Cu}(\text{NO}_3)_2 \cdot 3\text{H}_2\text{O}$, 99%, Aladdin), sodium hydroxide (NaOH , 98%, Aladdin) and deionized water (H_2O). All of the chemicals were used without purification.

2.2 The synthesis of M/CeO_2

M/CeO_2 was synthesized *via* a three-step method, as shown in Fig. 1. In step I, firstly, 0.05 g of PVP, 2.17 g of $\text{Ce}(\text{NO}_3)_3 \cdot 6\text{H}_2\text{O}$,

and 2.10 g of $\text{H}_3\text{-BTC}$ were dissolved in 10 mL of ethanol, 50 mL of ethanol, and 100 mL of DMF-ethanol mixture ($V/V = 1:1$), respectively. Next, the PVP solution and $\text{Ce}(\text{NO}_3)_3$ solution were dropwise added to the $\text{H}_3\text{-BTC}$ solution under vigorously stirring. Then, the reaction was conducted at 80°C for 20 h. After the reaction, the white solid (Ce-BTC) was centrifuged and washed by ethanol for three times before being dried at 60°C for 24 h. Finally, the Ce-BTC was obtained. In step II, firstly, 0.1 mmol of metal acetylacetonate ($\text{M}(\text{acac})_x$, $\text{M} = \text{Cu}$, Ni , Co , and Fe) was dissolved in 15 mL of ethanol. Then, 0.5 g of Ce-BTC was added to the above solution, and the solid-liquid mixture was fully stirred for 24 h at room temperature. Finally, the ethanol was evaporated at 80°C to obtain the solid ($\text{M}/\text{Ce-BTC}$). In step III, the obtained Ce-BTC and $\text{M}/\text{Ce-BTC}$ were calcined at 500°C for 5 h in the air atmosphere to obtain CeO_2 and M/CeO_2 .

2.3 The catalytic performances for CO oxidation

The catalytic performances of the prepared samples for CO oxidation were evaluated in a quartz tube (inner diameter = 7 mm) fixed-bed microreactor, as shown in Fig. S1.† The quartz tube loading 130 mg of the sample was placed vertically in a tube furnace. Four different kinds of feed gas (dry condition: 1 vol% CO, 4 vol% O_2 , N_2 balance, 20 mL min^{-1} , weight hourly space velocity (WHSV) of $9230\text{ mL g}^{-1}\text{ h}^{-1}$; wet condition: 1 vol% CO, 4 vol% O_2 , 5 vol% H_2O , N_2 balance, 20 mL min^{-1} , WHSV of $9230\text{ mL g}^{-1}\text{ h}^{-1}$; H_2 -rich condition: 75 vol% H_2 , 1 vol% O_2 , 0.25 vol% CO, N_2 balance, 40 mL min^{-1} , WHSV of $18\,460\text{ mL g}^{-1}\text{ h}^{-1}$; wet and H_2 -rich conditions: 75 vol% H_2 , 5 vol% H_2O , 1 vol% O_2 , 0.25 vol% CO, N_2 balance, 40 mL min^{-1} , WHSV of $18\,460\text{ mL g}^{-1}\text{ h}^{-1}$) passed through the quartz tube. The outlet of the reactor was connected with the gas chromatograph (GC-9160, Quhua, China) to record the compositions of mixed gas online. Before the catalytic performance test, the sample was pretreated with feed gas at 300°C for 2 h. The CO conversion, O_2 selectivity to CO_2 , and CO selectivity to CO_2 can be calculated according to eqn (1)–(3):

$$X_{\text{CO}} = ([\text{CO}]_{\text{in}} - [\text{CO}]_{\text{out}})/[\text{CO}]_{\text{in}} \times 100\% \quad (1)$$

$$S_{\text{O}_2} = 0.5[\text{CO}_2]_{\text{out}}/([\text{O}_2]_{\text{in}} - [\text{O}_2]_{\text{out}}) \times 100\% \quad (2)$$

$$S_{\text{CO}} = [\text{CO}_2]_{\text{out}}/([\text{CO}]_{\text{in}} - [\text{CO}]_{\text{out}}) \times 100\% \quad (3)$$

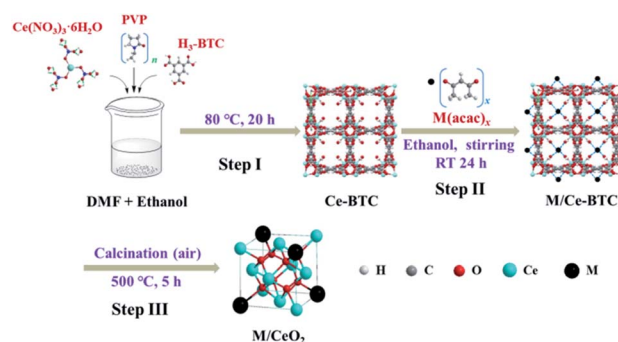


Fig. 1 The preparative route of M/CeO_2 .



where $[\text{CO}]_{\text{in}}$ and $[\text{CO}]_{\text{out}}$ represent CO concentration at the inlet and outlet, respectively. $[\text{O}_2]_{\text{in}}$ and $[\text{O}_2]_{\text{out}}$ are O_2 concentration at the inlet and outlet. $[\text{CO}_2]_{\text{out}}$ is CO_2 concentration at the outlet.

2.4 Characterization methods

The textural properties of the samples were measured by Autosorb-iQ-MP-AG gas adsorption instrument (Quantachrome Corporation). Except for Ce-BTC, the samples were pretreated at 300 °C for 3 h under the high vacuum condition before being measured. The Ce-BTC was pretreated at 150 °C for 8 h under the high vacuum condition. For all samples, the surface area was calculated by Brunner–Emmet–Teller (BET) method, the average pore diameter was calculated by Barrett–Joyner–Halenda (BJH) method, and the total pore volume was obtained over the P/P_0 value of 0.99. The crystal structures and properties were determined by XRD using the Rigaku Smart Lab operating at 30 mA and 40 kV with a Cu K α radiation ($\lambda = 1.5418 \text{ \AA}$). The scan speed of $10^\circ \text{ min}^{-1}$ was applied in each continuous run at the 2θ range of 10° to 70° , except for Ce-BTC (5° to 70°). The average crystallite size was obtained by Scherrer equation ($D_\beta = K\lambda/(\beta \cos \theta)$), λ is the wavelength ($\lambda = 1.5418 \text{ \AA}$), K is the particle shape factor ($K = 0.89$), β is the full-width at half maximum height in radians, and θ is the diffraction angle). The metal contents (Ce, Cu, Ni, Co, and Fe) in the catalysts were determined by ICP-OES on the Agilent 720ES. The thermal stability was analyzed by TGA (Mettler Toledo) in the air (flow rate: 120 mL min^{-1}) at a ramping rate of $10^\circ \text{ C min}^{-1}$. The morphological structures were investigated by SEM (Hitachi, SU5000), TEM (JOEL, JEM2100), and HRTEM (Philips, C/M300). X-ray energy dispersive spectra (EDX) were also performed on TEM equipped with the corresponding accessories. The surface chemistry was analyzed by XPS (AXIS-His, Kratos Analytical). The C 1s core level peak with binding energy at 284.8 eV was taken as energy calibration. The reducibility of components was analyzed by H_2 -TPR which was carried out in Micromeritics Autochem II 2920 equipped with the thermal conductivity detector (TCD). The sample was pretreated at 300 °C with 20 mL min^{-1} of He gas for 2 h. The test was performed from room temperature to 850 °C with a heating rate of $10^\circ \text{ C min}^{-1}$. *In situ* DRIFTS was adopted to study the reaction process of CO oxidation using the Thermo Scientific Nicolet iS50 spectrometer which was equipped with a KBr optical beam and a Mercury–Cadmium–Telluride (MCT) detector scanning in the wavenumber range of 4000 cm^{-1} to 650 cm^{-1} . Each sample was placed into an infrared cell equipped with Zn–Se window. Before testing, the sample was purged by N_2 stream (30 mL min^{-1}) at 300 °C for 30 min to remove the adsorbed water and other volatile components, and then cooled to the targeted temperature for obtaining the background spectrum. The test process was divided into three stages. Firstly, the sample was exposed to the CO stream with a flow rate of 30 mL min^{-1} for 30 min to reach surface saturation. Then, the N_2 stream passed through the sample with a flow rate of 30 mL min^{-1} for 30 min. Finally, the atmosphere was switched to O_2 gas with a flow rate of 30 mL min^{-1} for 30 min.

3. Results and discussion

3.1 CO oxidation ability and catalyst stability

The catalytic performances of prepared samples for CO oxidation in the dry condition were shown in Fig. 2A. It can be seen that the temperature at 100% CO conversion (T_{100}) increases in the sequence of Cu/CeO_2 (100 °C) < Ni/CeO_2 (160 °C) < Co/CeO_2 (180 °C) < Fe/CeO_2 (260 °C) < CeO_2 (290 °C), suggesting that the doping of Cu, Ni, Co, or Fe on CeO_2 can significantly promote the catalytic activity. Among the catalysts investigated, Cu/CeO_2 exhibits the best catalytic performance, which may be due to high oxygen vacancy, and high CO adsorption capacity ($\text{Cu}^+ - \text{CO}$) (*vide infra*). Furthermore, the catalytic activity of Cu/CeO_2 is much higher than those of bare CuO (derived from the calcination of $\text{Cu}(\text{acac})_2$, 500 °C for 5 h) and bare CeO_2 , which indicates there exists a strong interaction between Cu and CeO_2 to improve the catalytic activity. To obtain meaningful kinetics, the CO conversion data <15% which can ignore the heat and mass transport effects were used to calculate the activation energy (E_a), as shown in Fig. 2B. It can be found that the E_a over Cu/CeO_2 (53.3 kJ mol^{-1}) is much lower than those catalyzed by other metal oxides, indicating the high catalytic activity for CO oxidation, which is consistent with the result of Fig. 2A. Interestingly, although the E_a over Ni/CeO_2 is higher than that over Co/CeO_2 , Ni/CeO_2 exhibits better catalytic performance. It may be due to the fact that the pre-exponential factor value of Ni/CeO_2 ($1.19 \times 10^{11} \text{ h}^{-1}$) was much higher than that of Co/CeO_2

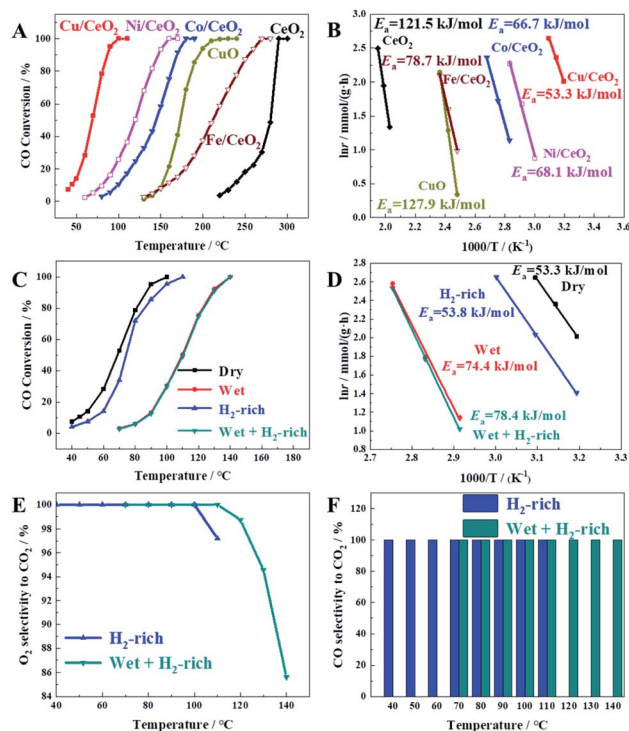


Fig. 2 (A and B) The CO conversion data and the corresponding Arrhenius plots under the catalysis of six different catalysts in dry condition. (C and D) The CO conversion data and the corresponding Arrhenius plots over Cu/CeO_2 using four gas mixtures as feedstock. (E) O_2 selectivity to CO_2 . (F) CO selectivity to CO_2 .



($2.24 \times 10^{10} \text{ h}^{-1}$), which suggests a higher density of active sites for the CO oxidation.²⁰

Furthermore, we also investigated the catalytic activity of Cu/CeO₂ prepared by co-precipitation (defined as Cu/CeO₂(cp)), as shown in Fig. S2.† It can be seen clearly that Cu/CeO₂ exhibited higher catalytic activity than that of Cu/CeO₂(cp) in CO oxidation, which indicated the advantages of the method being used.

The actual CO treatment gas, like the reformer gas, usually contains a large amount of hydrogen (H₂) and an appropriate amount of water vapor (H₂O), so it is necessary to investigate the catalytic activity of the prepared catalyst for CO oxidation under the atmosphere of H₂, H₂O and the both. Herein, we investigated the catalytic activity of Cu/CeO₂ for CO oxidation in wet, H₂-rich, and wet + H₂-rich conditions, respectively. As shown in Fig. 2(C and D), CO is completely converted at 140 °C under 5.00 vol% H₂O (wet condition), exhibiting a delay of 40 °C in comparison with catalytic activity in dry condition, which may be caused by the H₂O blocking for the active sites or the competitive adsorption between H₂O and O₂.^{24,26} Accordingly, the E_a (74.4 kJ mol⁻¹) in the wet condition is much higher than that (53.3 kJ mol⁻¹) in the dry condition. The complete conversion of CO is achieved at 110 °C in H₂-condition, showing only 10 °C of delay compared to dry condition, and their E_a are extremely similar (53.3 kJ mol⁻¹ and 53.8 kJ mol⁻¹), which suggests the reaction mechanism of CO oxidation is not changed with the existence of H₂. Similarly, the existence of H₂ has little effect on the CO conversion in wet conditions judging from the CO conversion curve and E_a . It can be seen clearly from Fig. 2E that when the reaction temperature is too high, O₂ selectivity to CO₂ is less than 100% in H₂-rich conditions due to the competitive oxidation of H₂. Furthermore, at 110 °C, the value of O₂ selectivity in wet and H₂-rich conditions is 100%, while it is 97.20% in H₂-rich condition, indicating the presence of water also prevents the oxidation of H₂ due to the H₂O cover for active sites. In Fig. 2F, all of CO selectivity to CO₂ are 100%, which suggests the reaction of CO and H₂ is non-existent due to the low reaction temperature range. The obtained results reveal that the prepared Cu/CeO₂ is highly active for CO oxidation.

The stability of prepared Cu/CeO₂ for CO oxidation under four different gas atmospheres was also investigated by the

time-on-stream studies, as shown in Fig. 3. It is obvious that no discernible decrease occurred in CO conversion, which suggested the prepared Cu/CeO₂ is quite stable. In addition, the catalytic performances of Cu/CeO₂ for CO oxidation were compared with those reported in the literature, summarized in Table S1.† It can be concluded that the prepared Cu/CeO₂ exhibits the superior catalytic activity to many other catalysts due to the lower T_{100} . Therefore, the prepared Cu/CeO₂ can be an excellent catalyst for CO oxidation.

3.2 Characterization results

N₂ adsorption-desorption isotherms and pore size distributions of the prepared samples were displayed in Fig. 4(i) and S3,† and the corresponding textural properties were given in Table 1. All the isothermal curves exhibit the typical IV-type behavior, and have the H3 type hysteresis loop over P/P_0 value of 0.50 to 0.99, which indicates the existence of mesopores. Accordingly, the pore size distributions of the samples are mainly concentrated on 4 nm. It can be found that the BET surface area and total pore volume of Ce-BTC are much less than those of CeO₂ and M/CeO₂. The explanations for the result are that some of DMF molecules remain in the pore of Ce-BTC, which can be demonstrated by FT-IR, as shown in Fig. S4† (the peaks at 2973 cm⁻¹, 2875 cm⁻¹, and 1659 cm⁻¹ are attributed to $\nu_{\text{as}}(-\text{CH}_3)$, $\nu_{\text{s}}(-\text{CH}_3)$ and $\nu(\text{C}=\text{O})$ of DMF, respectively²⁷), and after calcination, the DMF and organic ligands are removed from the Ce-BTC to form CeO₂ or M/CeO₂, making more space. Besides, the average pore diameter of Ce-BTC and obtained metal oxides is similar, which suggests the corresponding derivative oxide products maintain the superior pore structure.

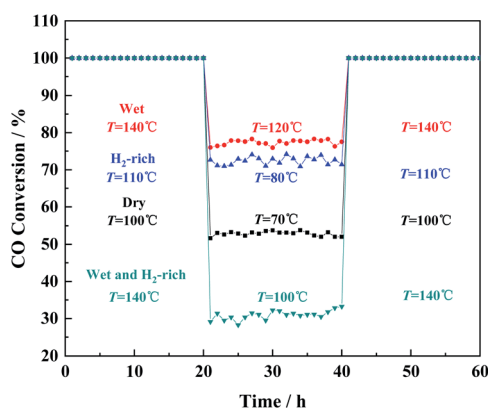


Fig. 3 The long-term stability of Cu/CeO₂ in CO oxidation under the four gas atmospheres.

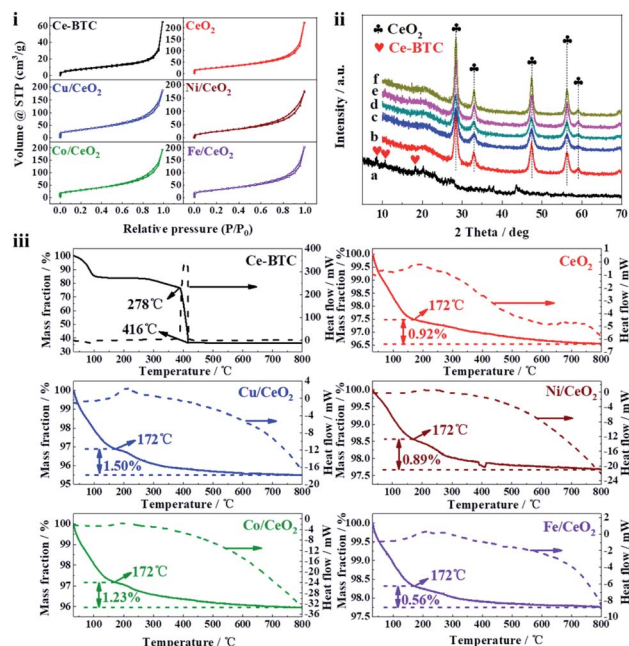


Fig. 4 (i) N₂ adsorption-desorption isotherms of the prepared samples. (ii) The XRD patterns of the prepared samples: (a) Ce-BTC, (b) CeO₂, (c) Co/CeO₂, (d) Cu/CeO₂, (e) Fe/CeO₂, (f) Ni/CeO₂. (iii) TGA (air atmosphere) and heat flow curves of prepared samples.



Table 1 Textural/structural properties of the prepared samples

Sample	Textural analysis			XRD analysis	ICP-OES
	BET surface area ($\text{m}^2 \text{g}^{-1}$)	Pore volume ($\text{cm}^3 \text{g}^{-1}$)	Average pore size (nm)	Average crystallite size ^a (nm)	Metal content (wt%)
Ce-BTC	25.90	0.10	3.83	10.32	—
CeO ₂	94.75	0.34	3.42	9.49	Ce: 81.77
Cu/CeO ₂	114.09	0.29	3.42	7.49	Ce: 77.37
					Cu: 4.09
Ni/CeO ₂	86.71	0.27	3.83	11.85	Ce: 76.95
					Ni: 4.44
Co/CeO ₂	105.61	0.30	3.41	7.00	Ce: 77.30
					Co: 3.66
Fe/CeO ₂	108.72	0.31	3.82	10.21	Ce: 78.84
					Fe: 2.09

^a Calculated by Scherrer equation.

The XRD patterns of the prepared samples were shown in Fig. 4(ii), and the corresponding average crystallite size calculated by Scherrer equation was presented in Table 1. For Ce-BTC, the peaks appear at 8.48° , 10.64° , and 18.18° are consistent with the previous reports,^{28,29} which suggests that Ce-BTC has been prepared successfully. Regarding the metal oxides, they all exhibit the fluorite type cubic CeO₂ phase (28.34° (111), 33.06° (200), 47.36° (220), 56.35° (311), and 59.06° (222)). Interestingly, no peaks belonging to transition metals (M species) are observed, and it is similar to the previous study,^{4,30} which indicates M species have been successfully doped into CeO₂.⁴ More or less the same crystallite size for CeO₂ and M/CeO₂ suggests that the addition of M does not affect the structural characteristics of CeO₂ (also can be seen in SEM and TEM). The ICP-OES result (Table 1) reveals that the content of M in the prepared samples is less than 5 wt%, however, the little amount of M plays a significant role in the improvement of catalytic activity (Fig. 2B). In addition, the difference of M content in the prepared samples may cause by the different adsorption capability of Ce-BTC towards the different M(acac)_x.

TGA was further employed to determine the thermal stability of prepared samples, as shown in Fig. 4(iii). In all samples, the weight loss before 150°C can be attributed to the volatilization of sample adsorbates, like water. The Ce-BTC skeleton decomposes rapidly from 386°C to 416°C , which is associated with a strong exothermic peak in the heat flow curves. After 416°C , Ce-BTC is basically converted into CeO₂, indicating the calcination temperature (500°C) for sample preparation is enough. For CeO₂ and M/CeO₂, it can be seen clearly that when the temperature rises from 172°C to 800°C , all of the weight losses are lower than 1.50%, which suggests they possess high thermal stability.

The morphological structures of the prepared samples were characterized by SEM and TEM, as shown in Fig. 5 and S5.† It is clearly that the morphology of Ce-BTC presents a straw-like bundle structure, which is quite different from those reported by Zhang (cauliflower-like structure, strawsheave-like structure, and rod-like structure).^{28,30,31} Compared to Ce-BTC, the surface

morphologies of CeO₂ and M/CeO₂ become rougher and more shriveled due to the calcination, but they still maintain the bundle structure. The EDX elemental maps of Cu/CeO₂ (Fig. 5(f and g)) reveal that both Ce and Cu are uniformly distributed in the whole structure, which indicates Ce-BTC adsorbing with Cu(acac)₂ and then calcination is an effective method to prepare Cu/CeO₂ bimetallic oxides. Furthermore, in Fig. 5(i), the inter-layer distance between adjacent planes is calculated to be 0.31 nm, which can be indexed to the (111) crystal planes of CeO₂, being highly consistent with the XRD result.

H₂-TPR experiments were carried out to study the redox properties of bare CeO₂, bare CuO, and Cu/CeO₂, as shown in Fig. 6. The reduction profiles of bare CeO₂ consists of two broad overlapping peaks centered at 431.2°C and 517.3°C , and one peak at 788.3°C , which are attributed to the reaction of surface oxygen (O_s) from different crystal planes (overlapping peaks),

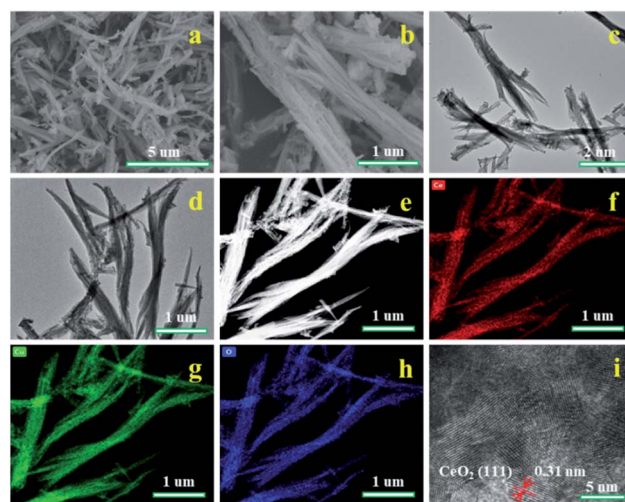


Fig. 5 (a and b) SEM images at different magnifications of Cu/CeO₂. (c and d) TEM images at different magnifications of Cu/CeO₂. (e–h) The dark-field TEM and the corresponding EDX elemental maps of Cu/CeO₂. (i) HRTEM image of Cu/CeO₂.



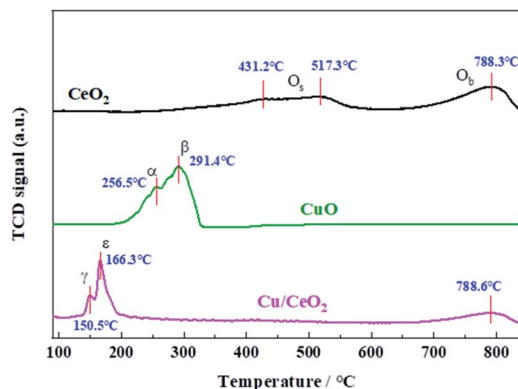


Fig. 6 The H_2 -TPR profiles of CeO_2 , CuO , and Cu/CeO_2 .

and bulk oxygen (O_b) of CeO_2 , respectively.^{1,32} Bare CuO has two overlapping peaks (α and β) at 256.5 °C and 291.4 °C, also being ascribed to the reduction of O_s and O_b , respectively. The reduction profiles of Cu/CeO_2 show two overlapping peaks (α and β) in the range of 150.5–166.3 °C, and one peak at 788.6 °C which is assigned to the reduction of Ce^{4+} into Ce^{3+} . The peak γ (150.5 °C) is assigned to the reduction of the uniformly dispersed CuO_x species interacting strongly with the CeO_2 surface, while the peak ϵ is attributed to the reduction of larger CuO_x species associated with Ceria.^{7,30,32,33} It can be found that the reduction of Cu/CeO_2 is easier than those of bare CuO and CeO_2 , indicating the strong interaction between CuO_x species and CeO_2 that facilitates the electron exchanges of $\text{Cu}^{2+}/\text{Cu}^+$ and $\text{Ce}^{3+}/\text{Ce}^{4+}$ ($\text{Ce}^{4+} + \text{Cu}^+ \rightleftharpoons \text{Ce}^{3+} + \text{Cu}^{2+}$),^{34,35} which weakens the metal–oxygen bonds and promotes the oxygen vacancy. The previous studies have revealed that the oxygen of CeO_2 is involved in the CO oxidation,^{3,33} therefore, the weakening of metal–oxygen bonds by Cu doping makes the oxygen of prepared catalyst combine with CO to form CO_2 easier, improving the catalytic activity.

XPS was used to analyze the elementary oxidation states of CeO_2 , M/CeO_2 , and CuO . In Fig. 7A, it is clearly that two different metals are included in M/CeO_2 . The C 1s spectra exhibited in Fig. 7B has two independent peaks (288.6–287.5 eV and 284.8 eV), which are assigned to the carboxylate carbon ($-\text{COO}$) and the sp^3 -carbon, respectively. The existence of carboxylate carbon suggests that the organics are not completely decomposed in the calcination process.^{23,36} Fig. 7C depicts the O 1s of the prepared samples, which can be divided into three main peaks, at 533.3 eV, 531.4 eV, and 529.8–529.4 eV, respectively. The first peak reveals the existence of hydroxyl groups and C–O (from the carboxyl group), which is consistent with the C 1s result. The second peak can be attributed to the surface adsorbed oxygen (O_{abs}), which is closely associated with the oxygen vacancies. The last peak is assigned to the lattice oxygen (O_{lat}).^{35,37} Fig. 7D displays the XPS spectra of the different doping metals. The two independent peaks located at 931.7 eV and 934.0 eV in $\text{Cu } 2\text{p}_{3/2}$ are attributed to the Cu^+ (Cu_2O) and Cu^{2+} (CuO), and the typical shake-up satellite at 942 eV is caused by the divalent Cu^{2+} species.^{7,38} In $\text{Ni } 2\text{p}_{3/2}$, the major peaks located at 853.7 eV and 856.3 eV are assigned to

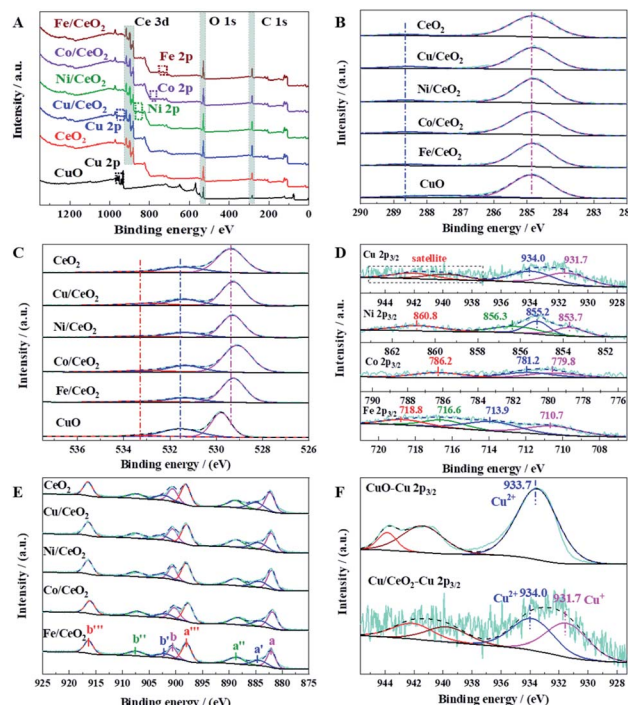


Fig. 7 XPS characterization results: (A) survey XPS spectra, (B) C 1s XPS spectra, (C) O 1s XPS spectra, (D) XPS spectra of the doping metals, (E) Ce 3d XPS spectra, (F) Cu $2\text{p}_{3/2}$ XPS spectra of CuO and Cu/CeO_2 .

NiO and Ni_2O_3 , respectively. The peak at 855.2 eV indicates surface Ni^{3+} species associated to the presence of Ni^{2+} vacancies in NiO crystal lattices.³⁹ Also, it is found that the satellite peak of NiO appears at 860.8 eV.⁴⁰ There are three peaks in $\text{Co } 2\text{p}_{3/2}$, which can be attributed to Co^{3+} (779.8 eV), Co^{2+} (781.2 eV), and the satellite peak of Co^{2+} (786.2 eV).⁴¹ In $\text{Fe } 2\text{p}_{3/2}$ region, Fe^{2+} and the satellite are characterized by the peak at 710.7 eV and 716.6 eV, respectively, while Fe^{3+} is characterized by the peak at 713.9 eV, with a strong satellite at 718.8 eV.^{37,42} The complex spectra of Ce 3d (Fig. 7E) are composed of eight peaks, namely at a (882.2 eV), a' (884.8 eV), a'' (888.7 eV), a''' (898.0 eV), b (900.6 eV), b' (903.2 eV), b'' (907.6 eV), and b''' (916.4 eV), as reported in several relevant studies.^{43,44} The six peaks a , a' , a'' , b , b' and b''' are the characteristics of Ce^{4+} ion on the $3\text{d}^{10}4\text{f}^0$ structure, whereas a' and b' are attributed to Ce^{3+} ion on the $3\text{d}^{10}4\text{f}^1$ structure. The co-existence of Ce^{3+} and Ce^{4+} indicates the formation of oxygen vacancy on the ceria surface, and the proportion of Ce^{3+} calculated from the area ratio of Ce^{3+} species to that of total Ce species ($\text{Ce}^{3+}/(\text{Ce}^{3+} + \text{Ce}^{4+})$) can represent the amount of surface oxygen vacancy. Among the samples investigated, the proportion of Ce^{3+} decreases in the sequence of Cu/CeO_2 (17.6%) > Ni/CeO_2 (17.3%) > CeO_2 (16.6%) > Fe/CeO_2 (16.4%) > Co/CeO_2 (15.4%). The fact that the oxygen vacancy of Cu/CeO_2 is higher than that of CeO_2 indicates the interaction between CuO_x and CeO_2 promotes the oxygen vacancy. The highest oxygen vacancy of Cu/CeO_2 is perfectly matched to its highest catalytic performance, suggesting the key role of oxygen vacancy on CO oxidation performance. Furthermore, the existence of oxygen vacancy was also revealed by Raman spectrum,



as shown in Fig. S6.† The band at 459 cm^{-1} is attributed to Raman active vibrational mode of fluorite-type CeO_2 , while that at 600 cm^{-1} is related to oxygen vacancy due to the presence of Ce^{3+} in the CeO_2 lattice.⁴⁵ The Cu $2p_{3/2}$ XPS spectra of CuO and Cu/CeO₂ were shown in Fig. 7F. It is clearly that Cu exists only in divalent state for CuO, while the co-existence of Cu^+ and Cu^{2+} is presented in Cu/CeO₂, which reveals the strong interaction between CuO_x and CeO₂ also can lead to a stable existence of Cu^+ in Cu/CeO₂. It is well recognized that Cu^+ has strong chemisorption to CO (*vide infra*), and the chemisorption of CO on Cu^+ is significant for CO oxidation.³⁵ Therefore, both high oxygen vacancy and high CO adsorption capacity contribute to the excellent catalytic activity of Cu/CeO₂ in CO oxidation.

In situ DRIFTS was adopted to study the reaction process of CO oxidation. Fig. 8a displays *in situ* DRIFTS of CO adsorption, N₂ purging, and O₂ dose over Cu/CeO₂ at 40 °C. Two intensive peaks at 2173 and 2115 cm^{-1} appear after CO feeding for 30 min, which can be attributed to the gas-phase CO.^{20,46} It can be found that the intensities of the two peaks decrease gradually when N₂ is introduced, suggesting that the non-chemically adsorbed CO is taken away under the N₂ flow. After N₂ purging, the characteristic peak of adsorbed CO appears at 2109 cm^{-1} , which reflects that the CO is adsorbed linearly on Cu^+ (Cu^+-CO).^{20,47} The peak intensity of adsorbed CO decreases rapidly after the introduction of O₂, indicating the rapid conversion of CO on the surface of Cu/CeO₂. Besides, the IR peaks in the range of 1700–1000 cm^{-1} are due to the diverse vibrations of carbonates and formates. For example, the peak at 1526 cm^{-1} represents the asymmetric stretch of formate species $\nu_{\text{as}}(\text{COO})$, and the symmetric stretch of carbonate species $\nu_{\text{s}}(\text{C}=\text{O})$ and formate species $\nu_{\text{s}}(\text{COO})$ are characterized by the peaks at 1627 and 1353 cm^{-1} , respectively. Fig. 8b depicts IR absorbance at 2115–2109 cm^{-1} along with time of N₂ purge over Cu/CeO₂ at different temperatures. It can be seen that at each temperature, the absorbance decreases with the increase of N₂ purge time, suggesting CO is constantly being taken away under the N₂ flow. The absorbance also decreases in the sequence of $T = 40\text{ °C} > T = 70\text{ °C} > T = 100\text{ °C}$, which reveals that the high temperature is unfavourable for the formation of Cu^+-CO , being in conformity with thermodynamic law. However, the high temperature can promote the reaction of CO and O₂. As shown in Fig. 8c, when O₂ is introduced into the system, the change rate of absorbance follows the sequence of $T = 100\text{ °C} > T = 70\text{ °C} > T = 40\text{ °C}$, which indicates that as the temperature increases, the conversion rate of CO to CO₂ increases, being in accordance with the law of reaction kinetics. The comprehensive effects of thermodynamics (CO absorption) and reaction kinetics (CO reaction) make CO conversion increase with the increase of temperature (Fig. 2A). The absorbance at 2115–2109 cm^{-1} along with time of N₂ purge over different samples at 40 °C were exhibited in Fig. 8d. It can be seen clearly that the absorbance decreases in the sequence of Cu/CeO₂ > Ni/CeO₂ > Co/CeO₂ > Fe/CeO₂ > CeO₂, suggesting the CO adsorption capacity of the investigated samples follows the above order. All of M/CeO₂ (Cu/CeO₂, Ni/CeO₂, Co/CeO₂, and Fe/CeO₂) show the higher absorption capacity of CO than that of CeO₂, indicating the introduction of M promotes CO accumulation degree on the

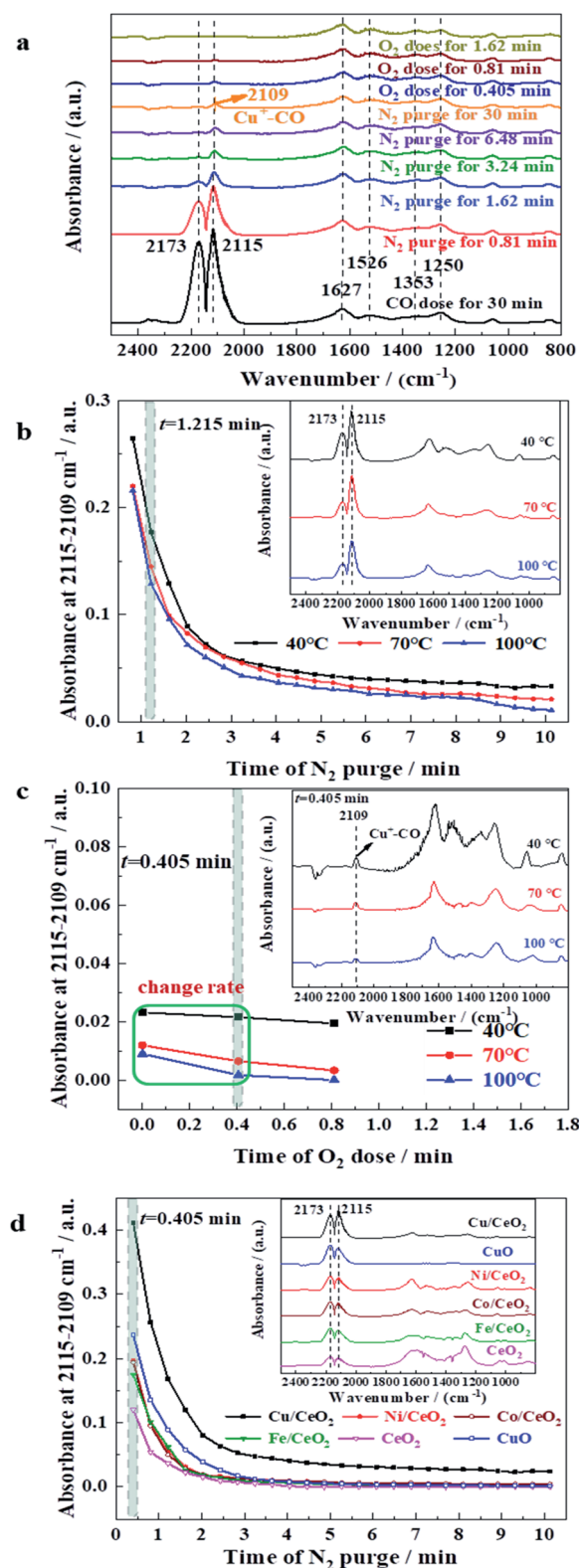


Fig. 8 (a) *In situ* DRIFTS of CO adsorption, N₂ purging, and O₂ dose over Cu/CeO₂ at 40 °C. (b) Absorbance at 2115–2109 cm^{-1} along with N₂ purge over Cu/CeO₂ at different temperatures. (c) Absorbance at 2115–2109 cm^{-1} along O₂ dose over Cu/CeO₂ at different temperatures. (d) Absorbance at 2115–2109 cm^{-1} along N₂ purge over different samples at 40 °C.

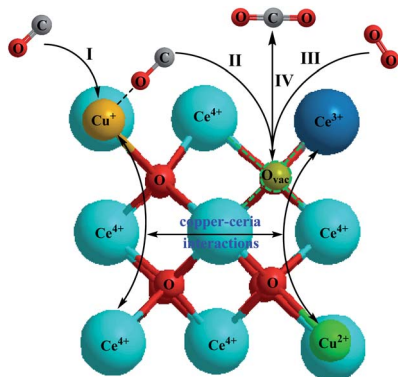


Fig. 9 A plausible mechanism for CO oxidation over Cu/CeO₂.

catalyst surface. Interestingly, the CO adsorption capacity is consistent with their catalytic activity in CO oxidation, which indicates CO adsorption capacity of doping metal determines the oxidation performance directly. In addition, compared to CuO, Cu/CeO₂ exhibits a better absorption capacity for CO, which is due to the stable existence of Cu⁺ derived from the strong interaction between CuO_x and CeO₂. Generally, in the reaction process of CO oxidation over Cu/CeO₂, the dispersed Cu⁺ promotes CO adsorption, and thus combines with oxygen on adjacent oxygen vacancy rapidly to form CO₂.

H₂-TPR, XPS, and *in situ* DRIFTS have revealed that the electron exchanges of Cu²⁺/Cu⁺ and Ce³⁺/Ce⁴⁺ pairs promote the oxygen vacancy and lead to the stable existence of Cu⁺ (improve CO absorption), which benefit the CO oxidation. Based on the results, we proposed a plausible mechanism for CO oxidation over Cu/CeO₂, as illustrated in Fig. 9, which involves four consecutive steps: (I) CO is adsorbed on the Cu⁺ to form Cu⁺-CO. (II) The chemisorbed CO (Cu⁺-CO) migrates to the metal-support interface. (III) O₂ is activated on oxygen vacancy of CeO₂ to form O₂⁻ (active oxygen) or O²⁻ (lattice oxygen). (IV) The chemisorbed CO reacts with active oxygen to form CO₂, and CO₂ diffuses from the catalyst surface to gas bulk.

4. Conclusions

In this work, we have reported an effective method to prepared M/CeO₂ bimetallic oxides for catalytic oxidation of CO, by calcination of Ce-BTC adsorbing with M(acac)_x. The results of XRD, ICP-OES, and XPS indicate that the transition metals (M, M = Cu, Ni, Co, and Fe) are successfully doped into CeO₂. TGA reveals that M/CeO₂ catalysts possess high thermal stability. Among the prepared M/CeO₂, Cu/CeO₂ performs the most excellent activity and high stability in CO oxidation under four different gas atmospheres. H₂-TPR, XPS, and *in situ* DRIFTS suggest that the electron exchanges of Cu²⁺/Cu⁺ and Ce³⁺/Ce⁴⁺ (Ce⁴⁺ + Cu⁺ ⇌ Ce³⁺ + Cu²⁺) facilitate the formation of active oxygen species and stabilize the Cu⁺ species (which improves CO adsorption), which make Cu/CeO₂ perform high catalytic activity in CO oxidation. In summary, this work has successfully designed the highly active and stable bimetallic oxide nanocomposites for CO oxidation, which has important implications

for the development of clean energy and environmental protection.

Conflicts of interest

There are no conflicts to declare.

Acknowledgements

This work was supported by the National Natural Science Foundation of China (no. 21908073) and Start-Up Scientific Research Funds for Newly Recruited Talents of Huaqiao University (no. 605-50Y20015).

References

- 1 M. Carltonbird, S. Eaimsumang, S. Pongstabodee, S. Boonyuen, S. M. Smith and A. Luengnaruemitchai, *Chem. Eng. J.*, 2018, **344**, 545–555.
- 2 I. Lee and F. Zaera, *J. Catal.*, 2014, **319**, 155–162.
- 3 M. Wilklow-Marnell and W. D. Jones, *Mol. Catal.*, 2017, **439**, 9–14.
- 4 C. R. Jung, A. Kundu, S. W. Nam and H.-I. Lee, *Appl. Catal., B*, 2008, **84**, 426–432.
- 5 M.-C. Jo, G.-H. Kwon, W. Li and A. M. Lane, *J. Ind. Eng. Chem.*, 2009, **15**, 336–341.
- 6 M. P. Woods, P. Gawade, B. Tan and U. S. Ozkan, *Appl. Catal., B*, 2010, **97**, 28–35.
- 7 X. Guo and R. Zhou, *Catal. Sci. Technol.*, 2016, **6**, 3862–3871.
- 8 S. Dey, G. C. Dhal, D. Mohan and R. Prasad, *Materials Discovery*, 2017, **8**, 26–34.
- 9 S. Dey and G. C. Dhal, *Inorg. Chem. Commun.*, 2019, **110**, 107614.
- 10 R. Khobragade, D. Yearwar, N. Labhsetwar and G. Saravanan, *Int. J. Hydrogen Energy*, 2019, **44**, 28757–28768.
- 11 T. M. Nyathi, N. Fischer, A. P. E. York, D. J. Morgan, G. J. Hutchings, E. K. Gibson, P. P. Wells, C. R. A. Catlow and M. Claeys, *ACS Catal.*, 2019, **9**, 7166–7178.
- 12 S. D. Senanayake, N. A. Pappoe, T.-D. Nguyen-Phan, S. Luo, Y. Li, W. Xu, Z. Liu, K. Mudiyansele, A. C. Johnston-Peck, A. I. Frenkel, I. Heckler, D. Stacchiola and J. A. Rodriguez, *Surf. Sci.*, 2016, **652**, 206–212.
- 13 M. D. Porosoff, B. Yan and J. G. Chen, *Energy Environ. Sci.*, 2016, **9**, 62–73.
- 14 J. Liu, A. Zhang, M. Liu, S. Hu, F. Ding, C. Song and X. Guo, *J. CO₂ Util.*, 2017, **21**, 100–107.
- 15 G. Zhu, S. Wang, Z. Yu, L. Zhang, D. Wang, B. Pang and W. Sun, *Res. Chem. Intermed.*, 2019, **45**, 3777–3793.
- 16 W. Xie and F. Wan, *Chem. Eng. J.*, 2019, **365**, 40–50.
- 17 D. Liu, G. Li and H. Liu, *Appl. Surf. Sci.*, 2018, **428**, 218–225.
- 18 X. Ge, Z. Li, C. Wang and L. Yin, *ACS Appl. Mater. Interfaces*, 2015, **7**, 26633–26642.
- 19 Z. Huang, L. Fan, F. Zhao, B. Chen, K. Xu, S. F. Zhou, J. Zhang, Q. Li, D. Hua and G. Zhan, *Adv. Funct. Mater.*, 2019, **29**, 1903774.
- 20 B. Chen, X. Yang, X. Zeng, Z. Huang, J. Xiao, J. Wang and G. Zhan, *Chem. Eng. J.*, 2020, **397**, 125424.



- 21 P. Kustrowski, L. Chmielarz, R. Dziembaj, P. Cool and E. F. Vansant, *J. Phys. Chem. B*, 2005, **109**, 11552–11558.
- 22 A. Valente, A. M. Botelho do Rego, M. J. Reis, I. F. Silva, I. F. Ramos and J. Vital, *Appl. Catal., A*, 2001, **207**, 221–228.
- 23 L. Fan, F. Zhao, Z. Huang, B. Chen, S.-F. Zhou and G. Zhan, *Appl. Catal., A*, 2019, **572**, 34–43.
- 24 A. Arango-Díaz, J. A. Cecilia, J. Marrero-Jerez, P. Nuñez, J. Jiménez-Jiménez and E. Rodríguez-Castellón, *Ceram. Int.*, 2016, **42**, 7462–7474.
- 25 A. Arango-Díaz, E. Moretti, A. Talon, L. Storaro, M. Lenarda, P. Núñez, J. Marrero-Jerez, J. Jiménez-Jiménez, A. Jiménez-López and E. Rodríguez-Castellón, *Appl. Catal., A*, 2014, **477**, 54–63.
- 26 I. Dobrosz-Gómez, I. Kocemba and J. M. Rynkowski, *Catal. Lett.*, 2008, **128**, 297–306.
- 27 Z. Huang, F. Zhao, L. Fan, W. Zhao, B. Chen, X. Chen, S.-F. Zhou, J. Xiao and G. Zhan, *Mater. Des.*, 2020, **194**, 108881.
- 28 X. Zhang, F. Hou, Y. Yang, Y. Wang, N. Liu, D. Chen and Y. Yang, *Appl. Surf. Sci.*, 2017, **423**, 771–779.
- 29 M. M. Peng, M. Ganesh, R. Vinodh, M. Palanichamy and H. T. Jang, *Arabian J. Chem.*, 2019, **12**, 1358–1364.
- 30 Y. Wang, Y. Yang, N. Liu, Y. Wang and X. Zhang, *RSC Adv.*, 2018, **8**, 33096–33102.
- 31 X. Zhang, F. Hou, H. Li, Y. Yang, Y. Wang, N. Liu and Y. Yang, *Microporous Mesoporous Mater.*, 2018, **259**, 211–219.
- 32 M. Lykaki, E. Pachatouridou, E. Iliopoulou, S. A. C. Carabineiro and M. Konsolakis, *RSC Adv.*, 2017, **7**, 6160–6169.
- 33 M. Lykaki, E. Pachatouridou, S. A. C. Carabineiro, E. Iliopoulou, C. Andriopoulou, N. Kallithrakas-Kontos, S. Boghosian and M. Konsolakis, *Appl. Catal., B*, 2018, **230**, 18–28.
- 34 M. Konsolakis, *Appl. Catal., B*, 2016, **198**, 49–66.
- 35 L. Qi, Q. Yu, Y. Dai, C. Tang, L. Liu, H. Zhang, F. Gao, L. Dong and Y. Chen, *Appl. Catal., B*, 2012, **119–120**, 308–320.
- 36 L. Fan, K. Wang, K. Xu, Z. Liang, H. Wang, S. F. Zhou and G. Zhan, *Small*, 2020, e2003597, DOI: 10.1002/smll.202003597.
- 37 J. Ouyang, Z. Zhao, S. L. Suib and H. Yang, *J. Colloid Interface Sci.*, 2019, **539**, 135–145.
- 38 E. Moretti, L. Storaro, A. Talon, M. Lenarda, P. Riello, R. Frattini, M. d. V. M. de Yuso, A. Jiménez-López, E. Rodríguez-Castellón, F. Ternero, A. Caballero and J. P. Holgado, *Appl. Catal., B*, 2011, **102**, 627–637.
- 39 A. Cárdenas-Arenas, A. Quindimil, A. Davó-Quiñonero, E. Bailón-García, D. Lozano-Castelló, U. De-La-Torre, B. Pereda-Ayo, J. A. González-Marcos, J. R. González-Velasco and A. Bueno-López, *Appl. Catal., B*, 2020, **265**, 118538.
- 40 B. Li, B. Zhang, Q. Guan, S. Chen and P. Ning, *Int. J. Hydrogen Energy*, 2018, **43**, 19010–19018.
- 41 L. Óvári, S. Krick Calderon, Y. Lykhach, J. Libuda, A. Erdőhelyi, C. Papp, J. Kiss and H. P. Steinrück, *J. Catal.*, 2013, **307**, 132–139.
- 42 H. Ali-Löytty, M. W. Louie, M. R. Singh, L. Li, H. G. Sanchez Casalongue, H. Ogasawara, E. J. Crumlin, Z. Liu, A. T. Bell, A. Nilsson and D. Friebe, *J. Phys. Chem. C*, 2016, **120**, 2247–2253.
- 43 Y. Cui and W.-L. Dai, *Catal. Sci. Technol.*, 2016, **6**, 7752–7762.
- 44 C. Wang, Q. Cheng, X. Wang, K. Ma, X. Bai, S. Tan, Y. Tian, T. Ding, L. Zheng, J. Zhang and X. Li, *Appl. Surf. Sci.*, 2017, **422**, 932–943.
- 45 Y. Huang, B. Long, M. Tang, Z. Rui, M.-S. Balogun, Y. Tong and H. Ji, *Appl. Catal., B*, 2016, **181**, 779–787.
- 46 Y. Wang, D. Li, K. Li and R. Farrauto, *Appl. Catal., B*, 2020, **267**, 118363.
- 47 H. Wan, Z. Wang, J. Zhu, X. Li, B. Liu, F. Gao, L. Dong and Y. Chen, *Appl. Catal., B*, 2008, **79**, 254–261.

